# Supporting Information for "A quantitative comparison and validation of finite-fault models: The 2011 Tohoku-Oki earthquake"

**Jeremy Wing Ching Wong**[1], **Wenyuan Fan**[1], **Alice-Agnes Gabriel**[1,2]

[1]Scripps Institution of Oceanography, University of California San Diego, La Jolla, CA, USA
[2]Department of Earth and Environmental Sciences, Ludwig-Maximilians-Universität München, Munich , Germany

## Supplementary Contents

1. Text S1–S3
2. Table S1–S3
3. Figures S1–S24

Corresponding author: Jeremy Wing Ching Wong, wcwong@ucsd.edu

## Text S1: Overview of the 32 Finite-fault Slip Models

Model G1 is from Pollitz et al. (2011), which is obtained using geodetic measurements. The total moment of the model is $4.1\times10^{22}$ N·m, equivalent to a $M_w$ 9.01 earthquake. The model includes a total of 5151 subfaults, with 101 and 51 subfaults along the strike and dip directions, respectively. Each subfault has an area of $7 \times 4.5$ km$^2$. The model is parameterized as three planar faults with strike and dip as 195° and 10°, 195° and 14°, and 195° and 22° at the depth ranges of 3–21, 21–39, and 39–57 km. The rake angles of all subfaults are fixed at 90°. The model composes of two major slip patches located updip and downdip of the hypocenter in zones ZC1 and ZC2, with peak slip away from the trench.

Model G2 is from Ito et al. (2011), which is obtained using geodetic measurements. The total moment of the model is $4.1\times10^{22}$ N·m, equivalent to a $M_w$ 9.01 earthquake. The model includes a total of 525 subfaults, with 35 and 15 subfaults along the strike and dip directions, respectively. Each subfault has a varying area. The model is parameterized as a non-planar fault. The model composes of a single slip patch at the updip area in zone ZC1. The major slip patch is slightly south of the hypocenter, located between 37°N to 38°N.

Model G3 is from Diao et al. (2012), which is obtained using geodetic measurements. The total moment of the model is $2.3\times10^{22}$ N·m, equivalent to a $M_w$ 8.84 earthquake. The model includes a total of 288 subfaults, with 24 and 12 subfaults along the strike and dip directions, respectively. Each subfault has an area of $20\times20$ km$^2$. The model is parameterized as a non-planar fault. The model composes of a single smooth slip patch in zone ZC1.

Model G4 is from Iinuma et al. (2012), which is obtained using geodetic measurements. The total moment of the model is $4.0\times10^{22}$ N·m, equivalent to a $M_w$ 9.00 earthquake. The model includes a total of 806 subfaults, with 31 and 13 subfaults along the strike and dip directions, respectively. Each subfault is represented by bi-cubic B-spines with 20 km intervals. The model is parameterized as a non-planar fault. The model has the largest slip at the trench and extended along strike slip patch. The model consists of a secondary slip patch extending to the southern deeper region in zone S2.

Model G5 is from C. Wang et al. (2012), which is obtained using geodetic measurements and InSAR measurements. The total moment of the model is $3.2\times10^{22}$ N·m, equivalent to a $M_w$ 8.94 earthquake. The model includes a total of 1080 subfaults, with 60 and 18 subfaults along the strike and dip directions, respectively. Each subfault has an area of $11.7\times11.1$ km$^2$. The model is parameterized as a varying dip angle fault with a striking angle of 195°. The model has a single slip patch at the updip of the hypocenter in zone ZC1 with peak slip away from the trench.

Model G6 is from R. Wang et al. (2013), which is obtained from geodetic measurements and displacement from integrated strong ground motion waveforms. The total moment of the model is $2.9\times10^{22}$ N·m, equivalent to a $M_w$ 8.91 earthquake. The model includes 1920 subfaults with 64 subfaults along strike and 30 subfaults along dip. Each subfaults has a size of $10\times10$ km$^2$. The model is parameterized as a non-planar fault. The model composes of a single slip patch at the updip of the hypocenter in zone ZC1 with peak slip away from the trench.

Model G7 is from Zhou et al. (2014), which is obtained from probabilistic inversion of geodetic data. The total moment of the model is $3.8\times10^{22}$ N·m, equivalent to a $M_w$ 8.99 earthquake. The model includes 350 subfaults with 25 subfaults along the strike and 14 subfaults along the dip. Each subfault has a size of $25\times18$ km$^2$. The model is parameterized as a varying dipping angle fault with a striking angle of 201. The model has a horse-shoe-shaped slip patch surrounding the hypocenter with peak slip at the trench in zones ZC1 and ZC1.

Model G8 is from Hashima et al. (2016), which is obtained from geodetic measurements. The total moment of the model is $4.0\times10^{22}$ N·m, equivalent to a $M_w$ 9.00 earthquake. The model includes 256 subfaults with 32 along-strike subfaults and eight along-dip subfaults. Each subfaults has a varying subfault area. The model is parameterized as a non-planar fault. The rake angles of all subfaults are fixed with the incoming plate direction. The model has a board and smooth slip patch with slip peaking at the trench at the updip area of the hypocenter in zone ZC1.

Model G9 is from Xie and Cai (2018), which applies stress inversion formulation for slip distribution from geodetic measurements. The total moment of the model is $4.5\times10^{22}$ N·m, equivalent to a $M_w$ 9.04 earthquake. The model includes 140 subfaults with 20 along-strike subfaults and seven along-dip subfaults. Each subfaults has a 25 km×25 km subfault area. The model is parameterized as a non-planar fault. The model has a board and smooth slip patch with slip peaking at the trench in zone ZC1, with a slightly wider rupture than other geodetic models.

Model R1 is from Lee et al. (2011), which is inverted from regional broadband seismograms and geodetic measurements. The total moment of the model is $3.7\times10^{22}$ N·m, equivalent to a $M_w$ 8.98 earthquake. The model includes 396 subfaults with 33 along-strike subfaults and 12 along-dip subfaults. Each subfaults has a $20\times20$ km$^2$ subfault area. The model is parameterized as a planar fault with strike and dip as 195° and 14°, respectively. The model shows a single smooth, slightly elongated slip patch at the updip in zone ZC1 and towards the north of the hypocenter with peak slip away from the trench in zone N1.

Model R2 is from Suzuki et al. (2011), which is inverted from strong ground motion records. The total moment of the model is $4.4\times10^{22}$ N·m, equivalent to a $M_w$ 9.03 earthquake. The model includes 119 subfaults with 17 along-strike subfaults and seven along-dip subfaults. Each subfaults has a $30\times30$ km$^2$ subfault area. The model is parameterized as a planar fault with strike and dip as 195° and 13°. The model shows a single smooth, expanded, increasing slip from the hypocenter region to the trench in zone ZC1. The expanded slip reaches beyond 39°N in zone ZN1.

Model R3 is from Wei et al. (2012), which is inverted from strong ground motion records and geodetic measurements. The total moment of the model is $5.3\times10^{22}$ N·m, equivalent to a $M_w$ 9.08 earthquake. The model includes 273 subfaults with 21 along-strike subfaults and 13 along-dip subfaults. Each subfault has an area of $25\times20$ km$^2$. The model is parameterized as a planar fault with strike and dip as 201° and 10∘. The model shows a major slip patch in zone ZC1, with peak slip located away from the trench. Significant shallow slip extends to the southern ZS1 region, reaching 36°N.

Model R4 is from Yue and Lay (2013), which is inverted from high-rate geodetic data and teleseismic data. The total moment of the model is $4.2\times10^{22}$ N·m, equivalent to a $M_w$ 9.02 earthquake. The model includes 120 subfaults with 15 along strike subfaults and 8 along dip subfaults. Each subfaults has a size of $30\times30$ km$^2$. The model is parameterized as a dip-varying planar fault with the strike as 202°. The slip distribution is characterized by two major slip patches, with one located at the updip of the hypocenter in zone ZC1 and a similar one located at the down dip of the hypocenter in zone ZC1.

Model S1 is from Ide et al. (2011), which is inverted slip distribution from vertical broadband seismograms with a high-pass filter above 200 s with the empirical Green's function method. The total moment of the model is $4.5\times10^{22}$ N·m, equivalent to a $M_w$ 9.04 earthquake. The model includes 231 subfaults with 21 along-strike subfaults and 11 along-dip subfaults. Each subfaults consist of bilinear spline basis functions with 10 km node separation. The model is parameterized as a planar fault with strike and dip as 190 and 15.3. The model has a widespread slip distribution from the downdip at around 50 km

depth to the trench in zone ZC1 and ZC1. The near trench slip extends from 39.5°N to 36.5°s.

Model S2 is from Hayes (2011), which is the initial USGS model inverted from teleseismic body waves of P, SH with a period range of 1 to 200 s and surface waves in a period range of 200 to 500 s. The total moment of the model is $4.9 \times 10^{22}$ N·m, equivalent to a $M_w$ 9.06 earthquake. The model includes 325 subfaults with 25 along strike subfaults and 13 along dip subfaults. Each subfault has an area of $25 \times 20$ km$^2$. The model is parameterized as a planar fault with strike and dip as 194° and 10°. The model shows a major slip patch at the updip of the hypocenter in zone ZC1 and a secondary slip patch at the down-dip of the hypocenter in zone ZC1.

Model S3 is from the revised USGS finite-fault model of the Tohoku-oki earthquake, with the last update in 2018 (Goldberg et al., 2022). The model is inverted from teleseismic body waves of P, SH with a period range of 1 to 200 s and surface waves in the period range of 200 to 500 s. The total moment of the model is $4.8 \times 10^{22}$ N·m, equivalent to a $M_w$ 9.05 earthquake. The model has 325 subfaults, with 25 along strike subfaults and 13 along dip subfaults. The model is parameterized as a varying strike planar fault with strike and dip as 198 and 8, 198 and 15, and 198 and 21 at the depth ranges of 3–15, 15–33, and 33–52 km. The model shows a distinctive two major slip patch with one at the north of the hypocenter and one at the south of the hypocenter. The overall slip distribution is elongated along the strike with two minor deeper slip patches at the down-dip and north of the hypocenter in zone ZC1, reaching 50 km.

Model S4 is from Ammon et al. (2011), which is inverted from teleseismic P waves with relative source time function inverted from Rayleigh waves and high-rate GPS recordings. The total moment of the model is $3.6 \times 10^{22}$ N·m, equivalent to a $M_w$ 8.98 earthquake. The model has 560 subfaults, with 50 along strike subfaults and 14 along dip subfaults. Each subfault has a size of $15 \times 15$ km$^2$. The model is parameterized as a planar fault with strike and dip as 202° and 12°. The model shows a large smooth single-slip patch with peak slip extending from the hypocenter to the south of the hypocenter, located in the zone ZC1 and ZC1.

Model S5 is from Yagi and Fukahata (2011), which is inverted from teleseismic P waves in velocity with a period of 2.6 to 100 s. The total moment of the model is $5.7 \times 10^{22}$ N·m, equivalent to a $M_w$ 9.10 earthquake. The model has 250 subfaults with 25 along strike subfaults and 10 along dip subfaults. Each subfaults has a size of $10 \times 10$ km$^2$. The model is parameterized as a planar fault with strike and dip as 200 ° and 12°. The rake angles of all subfaults are fixed at 90 °. The model shows a major slip patch at the updip of the hypocenter, with the peak slip extending towards the trench in zone ZC1. Slip extends towards the south and deeper region in zone S2.

Model S6 is from Kubo and Kakehi (2013), which is inverted from teleseismic P waves with a period of 10 to 100 s. The total moment of the model is $3.4 \times 10^{22}$ N·m, equivalent to a $M_w$ 8.95 earthquake. The model has 108 subfaults with 18 along strike subfaults and six along dip subfaults. Each subfaults has a varying size. The model is parameterized as multiple planar faults with strike and dip 185° and 7 °, 197.5° and 11°, and 210° and 23° along strike. The model shows a very smooth slip patch with peak slip at the updip of the hypocenter reaching the trench in zone ZC1.

Model T1 is from Simons et al. (2011), which is inverted from tsunami and geodetic data. The total moment of the model is $7.8 \times 10^{22}$ N·m, equivalent to a $M_w$ 9.19 earthquake. The model has 419 subfaults with varying subfault sizes. The model is parameterized as a curved geometry triangulated by the subfaults. The model shows an elongated slip patch along the strike of the hypocenter in zones N1, ZC1 and ZC1. The elongated slip extends from 40° north to 37 °N. The model also shows a high level of heterogeneity with many smaller slip patches.

Model T2 is from Fujii et al. (2011), which is inverted from the tsunami data. The total moment of the model is $3.8\times10^{22}$ N·m, equivalent to a $M_w$ 8.99 earthquake. The model has 40 subfaults, with ten along strike subfaults and four along dip subfaults. Each subfault has a size of $50\times50$ km$^2$. The model is parameterized as a planar fault with strike and dip as 193° and 14°. The rake angles of all subfaults are fixed at 81°. The model shows a single and concentrated slip patch at the updip hypocenter region with slip increases towards the trench in zone ZC1.

Model T3 is from Saito et al. (2011), which is inverted from the tsunami data. The total moment of the model is $3.8\times10^{22}$ N·m, equivalent to a $M_w$ 8.99 earthquake. The model has 130 grid nodes, with 13 nodes along the strike and 10 nodes along the dip. Each node is represented by a Gaussian basis function. The model is parameterized as a varying dip fault with a strike of 193 °. The model shows a major slip asperity at the hypocenter region and extended slip towards the trench in zone ZC1.

Model T4 is from Gusman et al. (2012), which is inverted from tsunami and geodetic data. The total moment of the model is $5.1\times10^{22}$ N·m, equivalent to a $M_w$ 9.07 earthquake. The model has 45 subfaults with nine along strike and five along dip subfaults. Each subfault has a size of $50\times40$ km$^2$. The model is parameterized as a varying dip fault with a strike of 202°. The model shows a smooth single slip patch at the updip of the hypocenter with significant slip at the trench in zone ZC1.

Model T5 is from Hooper et al. (2013), which is inverted from tsunami and geodetic data. The total moment of the model is $4.0\times10^{22}$ N·m, equivalent to a $M_w$ 9.00 earthquake. The model has 234 subfaults with 18 along strike subfaults and 13 along dip subfaults. Each subfault has a size of 25 × 20 km$^2$. The model is parameterized as a dip varying fault with a strike of 194°. The model has a major slip patch at the updip of the hypocenter in zone ZC1. Narrow and elongated slip features from 20 km to 40 km extend near the hypocenter and towards the south of the hypocenter. A northern minor slip patch at the depth of 12 km in zone ZN1 also appears in the slip distribution.

Model T6 is from Satake et al. (2013), which is inverted from tsunami and geodetic data. The total moment of the model is $4.2\times10^{22}$ N·m, equivalent to a $M_w$ 9.02 earthquake. The model has 55 subfaults, with 11 along strike subfaults and five along dip sub faults. Each subfault has a size of $50\times50$ km$^2$. The model is parameterized as a dip-varying planar fault with a strike of 193°. The model shows a smooth large expanding slip patch in the updip of the hypocenter with increasing slip toward the trench in zone ZC1.

Model T7 is from Romano et al. (2014), which is inverted from tsunami and geodetic data. The total moment of the model is $5.7\times10^{22}$ N·m, equivalent to a $M_w$ 9.10 earthquake. The model has 398 subfaults. The model is parameterized as a curved fault with the subfaults subdivided into patches of variable size: 24 km×14 km, 24 km×24 km, 35×35 km$^2$ at depth ranges of 2-15, 15-40, 40-60 km. The model shows a similar overall slip structure as model G6 with a large expanding slip patch in the updip of the hypocenter with increasing slip toward the trench in zone ZC1. The model shows a high level of slip heterogeneity with many small slip patches.

Model T8 is from Kubota et al. (2022), which is inverted from Tsunami and geodetic data. The total moment of the model is $5.1\times10^{22}$ N·m, equivalent to a $M_w$ 9.07 earthquake. The model has 434 subfaults triangulating the 3D fault surface, with the length of each side of the triangle about 10 km. The model shows a smooth large slip patch at the updip of the hypocenter with increasing slip towards the trench in zone ZC1. The model shows near trench slip at the northern section in zone ZN1 reaching 39.5°N.

Model J1 is from Yokota et al. (2011), which is jointly inverted from geodetic, strong ground motion, teleseismic and tsunami observations. The total moment of the model is $4.2\times10^{22}$ N·m, equivalent to a $M_w$ 9.02 earthquake. The model has 96 subfaults, with

16 along strike subfaults and five along dip subfaults. Each subfault has a size of 30× 30 km$^2$. A varying dip fault geometry is used with a strike angle of 200°. The model shows a concentrated slip at the hypocenter along the 20 km depth in zones ZC1 and ZC1. The slip extends to the north, reaching 39.5°N.

Model J2 is from Minson et al. (2014), which is jointly inverted from the tsunami and high-rate GPS data. The total moment of the model is $5.3\times10^{22}$ N·m, equivalent to a $M_w$ 9.08 earthquake. The model has 219 subfaults, with 24 along strike subfaults and nine along dip subfaults. Each subfault has a size of around 30×30 km$^2$. The model is parameterized as a varying dip fault with a strike of 194°. The model shows a major slip patch at the hypocenter in zones ZC1 and ZC1. Extensive near trench slip was also imaged by the model extending from 39°N to 37°N. The model also shows a higher level of slip heterogeneity with patches of slip across the major slip area and other parts of the fault.

Model J3 is from Bletery et al. (2014), which is inverted from the geodetic, high-rate geodetic, strong ground motion, teleseismic P (1.25-100 s) and SH waves (2.5-100 s) and tsunami data. The total moment of the model is $3.5 \times 10^{22}$ N·m, equivalent to a $M_w$ 8.96 earthquake. The model has 187 subfaults with varying subfault sizes. The model is parameterized as a curved fault. The model shows a patchy shallow slip distribution with most slip confined at the updip of the hypocenter region in zone ZC1. The near trench slip extends from 37°N to 39.3°N.

Model J4 is from Melgar and Bock (2015), which is inverted from the collocated seismogendetic recordings and tsunami data. The total moment of the model is $5.5 \times 10^{22}$ N·m, equivalent to a $M_w$ 9.09 earthquake. The model has 189 subfaults, with 21 along strike subfaults and nine along dip subfaults. Each subfault has a size of 25×25 km$^2$. The model is parameterized as a curved fault. The model shows a major slip patch at the updip of the hypocenter with a confined large slip at the shallowest 10 km section of the fault in zone ZC1. Small near trench slip patches also appear in 40°N and 36°N.

Model J5 is from Yamazaki et al. (2018), which is iteratively inverted from the geodetic, teleseismic and tsunami data. The total moment of the model is $4.0 \times 10^{22}$ N·m, equivalent to a $M_w$ 9.00 earthquake. The model has 240 subfaults with 20 along strike subfaults and 12 along dip subfaults. Each subfault has a size of 20×20 km$^2$. The model is parameterized as a varying dip fault. The model shows a major L shape slip patch at the updip of the hypocenter with a confined large slip at the shallowest 10 km section of the fault and extended slip to 20 km dip at the south of the hypocenter in zone ZC1. Secondary features of the slip include a near trench slip at 39.5 °N in zone ZN1 and slip reaching 40 km depth at 37 °N in zone S2.

## Text S2: Teleseismic Displacement Waveforms Sensitivity Analysis

We compute teleseismic synthetic waveforms using the single-time window method with an assumed slip-rate function. We systematically compare synthetics from different slip-rate functions with varying duration. We use cosine, triangular, and regularized Yoffe functions to compute the synthetics (Figure S6). We pair the slip-rate functions with the same peak-slip-rate-time distribution from model S3 model for a consistent comparison. The comparison with the observations is summarized in Table S2.

We find that the teleseismic synthetics are insensitive to the shape and duration of the slip-rate functions. The synthetics are highly similar to the observations, with a median $\geq$0.82 correlation coefficient for all slip-rate functions. Figure S10 compares the synthetics with Yoffe, cosine and triangle functions, all having the same rise-time of 16 s and duration of around 32 s. The synthetics show negligible differences, suggesting that teleseismic waveforms are insensitive to the shape of the slip-rate function, given similar rise-time and duration.

We further compare the teleseismic data sensitivity to the decay rate and duration of the slip-rate function. We apply the Yoffe function with the same-rise time but with extended durations (40, 28, and 55 s), as shown in Figure S6. The synthetics show highly similar shapes with varying amplitudes (Figure S11). Particularly, the synthetics of the Yoffe function with varying duration show the same peak and trough timing in the synthetic waveforms. Hence, teleseismic waveforms seem to have limited sensitivity to the variation of the Yoffe function, confirming that our method with regularized Yoffe function for all models can effectively describe the slip-rate function for computing the teleseismic synthetics.

We further examine the rupture propagation effects on the teleseismic waveforms. We compare and validate different models' peak-slip-rate-time (PSRT) distributions, which describe the rupture front evolution of the respective models. We use three different slip models: Models S3, S6, and J5, all of which use teleseismic waveforms to invert slip distributions. Model S3 uses the single-time window method to describe the slip-rate evolution, while models S6 and J5 use the multi-time window method. We extract the PSRT of each projected model and map it to the model S3 slip distribution at the 16 km scale. We use the uniform regularized Yoffe function for each subfault and align it with the peak-slip-rate time accordingly.

The three PSRT distributions agree on major slip episodes but show varying complexity (Figure S13). Models S3 and J3 show a relatively smooth and regular expansion in the first 50 s, followed by a complex and irregular pattern for the rest of the rupture, associated with the major slip patch in ZC1. In contrast, model S6 shows a consistently smooth PSRT evolution. This smooth evolution continues through the major rupture area but with an increasing rupture speed. All three models show similar peak-slip-rate timing in the major slip patch. They suggest that the peak–slip-rate time for the major slip patch ranges from 40–80 s.

Synthetics using the S6 and J3 PSRT distributions show satisfactory fitting with the observed seismograms (Figure S14), with both synthetics reaching a correlation coefficient of 0.75. Comparatively, we compute the synthetics of models S6 and S3 using a uniform Yoffe function aligned with their peak-slip-rate time, respectively. The resulting synthetics have correlation coefficients with the observations of 0.71 for model S6 and 0.73 for model J3. The slight decrease in correlation results from our simplification of the complex slip-rate function from the multi-time-window method. Nevertheless, our comparison validates that the teleseismic waveforms are sensitive to the rupture propagation effects, and the peak-slip-rate time distribution of model S3 is effective in describing the slip-rate evolution.

## Text S3: Teleseismic Velocity Sensitivity Analysis

Our teleseismic data validation test in Section 4.2 shows that teleseismic displacement data are insensitive to the small-scale slip features. The displacement synthetics of the body waves have a dominant period of 15–20 s, which corresponds to a 90–120 km wavelength (Figure 11). We further test the sensitivity of teleseismic velocity waveforms, which contain more higher-frequency signals than the displacement waveforms, with a dominant period of around 10 s for the body waves. We follow the same procedure in Section 4.2.

We find that the teleseismic velocity waveforms have additional sensitivity to the fault geometry as compared to the displacement waveforms (Figure S16). We investigate the slip-rate function effects on the teleseismic velocity waveforms following the same procedure in Section 4.2.2. Our tests show that the velocity records have limited sensitivity to the slip-rate function (Figures S19 and S20). We explore the rupture propagation effects on the teleseismic velocity waveforms. We compare the slip-rate onset time alignment with the original S3 model onset time, peak-slip-rate time, and constant rupture velocity. We find that rupture propagation has a strong impact on the teleseismic velocity synthetics. Figure S19 shows synthetics using the original onset time alignment and a uniform Yoffe slip-rate function, resulting in a correlation of 0.52, while the original projected model has a correlation of 0.76. The synthetics using the PSRT alignment and a uniform Yoffe slip-rate function fit the observed waveforms, with a correlation of 0.71 (Figure S18). Similar to the displacement waveforms, both the constant rupture speed and two-step rupture speed failed to produce reasonable waveform fits (Figure S18).

We also apply the PSRT approach using the PSRT distributions from models S6 and J3. Following the same procedure in Section 4.2.3, we compute the teleseismic velocity synthetics using the S3 slip distribution and the PRST distributions from models S6 and J3. Both sets of synthetics can fit the long-period waveforms but not the short-period signals (Figure S22). We compute synthetics using the PSRT from model S3 and the slip distributions from models S6 and J3. The synthetics are similar to those from the S3 slip distribution.

We follow the same procedure and compute teleseismic synthetics velocity waveforms using the final slip distributions at the 16, 32, and 64 km scales for all models. Figure S23 shows teleseismic body-wave velocity synthetics for all models at a 16 km scale. The synthetics fit the first-order features of the teleseismic velocity observations. For example, the synthetics show accurate peaks and troughs for SH and SV waves at station BRVK. However, synthetics variations are more significant in the teleseismic velocity waveforms than the displacement waveforms. Synthetics SH waves from different slip models show contrasting waveform shapes around 50–150 s from S wave arrivals at both stations COR and HNR. The variations in velocity waveforms suggest a possible higher sensitivity for secondary slip features. We compute the correlation coefficients of the synthetic body waves with the observations. The velocity seismic synthetics of all models at three scales show a lower correlation ranges from 0.5 to 0.7, with the SH synthetics slightly better than P and SV synthetics. However, it is worth noting that the correlation value of the velocity waveforms is also compatible with typical inversion results (e.g. Melgar & Bock, 2015).

**Table S1.** Offshore geodetic stations

| Station | Longitude | Latitude | Depth [km] | Eastward displacement [m] | Northward displacement [m] | Vertical displacement [m] |
|---|---|---|---|---|---|---|
| GJT3 | 143.483 | 38.273 | 3.281 | 29.500 | -11.000 | 3.734 |
| GJT4 | 142.833 | 38.407 | 1.445 | 14.000 | -5.000 | 3.500 |
| MYGI | 142.917 | 38.084 | 1.700 | 22.100 | -10.400 | 3.100 |
| MYGW | 142.433 | 38.153 | 1.100 | 14.300 | -5.100 | -0.800 |
| FUKU | 142.083 | 37.166 | 1.200 | 4.400 | -1.700 | 0.900 |
| KAMS | 143.263 | 38.636 | 2.200 | 21.100 | -8.900 | 1.500 |
| KAMN | 143.363 | 38.887 | 2.300 | 13.800 | -5.800 | 1.600 |
| CHOS | 141.670 | 35.500 | 1.600 | 0.950 | -0.950 | 0.400 |
| TJT1 | 143.796 | 38.209 | 5.758 | N.A. | N.A. | 5.093 |
| P02 | 142.502 | 38.500 | 1.100 | N.A. | N.A. | -0.801 |
| P06 | 142.584 | 38.634 | 1.250 | N.A. | N.A. | -0.975 |
| TM1 | 142.780 | 39.236 | 1.500 | N.A. | N.A. | -0.800 |
| TM2 | 142.446 | 39.256 | 1.000 | N.A. | N.A. | -0.300 |

**Table S2.** Summary of teleseismic P wave displacement synthetics performance on changing geometry, subfault size, slip-rate, and rupture front time-alignment.

| Slip model | subfault [a] | slip-rate[b] | slip-rate alignment[c] | P wave correlation [d] | P wave variance reduction [d] | Figure [e] |
|---|---|---|---|---|---|---|
| S3 | original | original | original | 0.90 (0.01) | 80% (5%) | FigS7 |
| S3 projected | original | original | original | 0.89 (0.01) | 68% (28%) | FigS7 |
| S3 projected | original | Yoffe16(40) | original | 0.84 (0.01) | 65% (15%) | FigS8 |
| S3 projected | original | Yoffe16(40) | S3 PSRT | 0.88 (0.01) | 74% (9%) | FigS8 |
| S3 projected | original | original | Vr 2.0 km/s | 0.65 (0.01) | 27% (30%) | FigS9 |
| S3 projected | original | original | Vr 1.5 &2.0 km/s | 0.65 (0.01) | 31% (12%) | FigS9 |
| S3 projected | original | Cosine16 | S3 PSRT | 0.88 (0.01) | 71% (18%) | FigS10 |
| S3 projected | original | Tri 16 | S3 PSRT | 0.88 (0.01) | 74% (11%) | FigS10 |
| S3 projected | original | Yoffe16(48) | S3 PSRT | 0.85 (0.01) | 71% (5%) | FigS11 |
| S3 projected | original | Yoffe16(55) | S3 PSRT | 0.82 (0.01) | 66% (2) | FigS11 |
| S3 projected | 16 km | Yoffe16(40) | S3 PSRT | 0.82 (0.01) | 63% (17%) | FigS12 |
| S6 projected | 16 km | Yoffe16(40) | S3 PSRT | 0.77 (0.03) | 47% (36%) | FigS12 |
| J3 projected | 16 km | Yoffe16(40) | S3 PRST | 0.76 (0.02) | 48% (17%) | FigS12 |
| G4 projected | 16 km | Yoffe16(40) | S3 PSRT | 0.76 (0.04) | 50% (24%) | FigS15 |
| R3 projected | 16 km | Yoffe16(40) | S3 PRST | 0.75 (0.04) | 48% (73%) | FigS15 |
| S3 projected | 16 km | Yoffe16(40) | S6 PSRT | 0.75 (0.03) | 49% (41%) | FigS14 |
| S3 projected | 16 km | Yoffe16(40) | J3 PSRT | 0.75 (0.02) | 54% (18%) | FigS14 |

[a] subfault size of the finite fault model, original S3 model subfault size is 25 km × 16.6 km

[b] Yoffe16(): Yoffe function with rise time 16s with duration in parentheses; Cosine16: Cosine function with rise time 16; Tri16: Triangle function with rise time 16. The slip-rate functions are shown in Figure S6

[c] Vr km/s - Rupture onset by constant rupture speed; Rupture onset - follow model rupture onset time; PSRT - peak slip rate time (Figure S5 and Figure S13).

[d] median (standard deviation)

[e] supplementary figure showing the synthetics and observed waveforms comparison

**Table S3.** Summary of teleseismic P wave velocity synthetics performance on changing geometry, subfault size, slip-rate, and rupture front time-alignment.

| Slip model | subfault [a] | slip-rate[b] | slip-rate alignment[c] | P wave correlation [d] | P wave variance reduction [d] | Figure [e] |
|---|---|---|---|---|---|---|
| S3 | original | original | original | 0.81 (0.01) | 55% (25%) | FigS16 |
| S3 projected | original | original | original | 0.76 (0.01) | 44% (65) | FigS16 |
| S3 projected | original | Yoffe16(40) | original | 0.52 (0.02) | 20% (1%) | FigS17 |
| S3 projected | original | Yoffe16(40) | S3 PSRT | 0.71 (0.02) | 50% (8%) | FigS17 |
| S3 projected | original | original | Vr 2.0 km/s | 0.48 (0.01) | 21% (2%) | FigS18 |
| S3 projected | original | original | Vr 1.5 &2.0 km/s | 0.54 (0.01) | 22% (24%) | FigS18 |
| S3 projected | original | Cosine16 | S3 PSRT | 0.74 (0.02) | 52% (21%) | FigS19 |
| S3 projected | original | Tri 16 | S3 PSRT | 0.72 (0.02) | 50% (8%) | FigS19 |
| S3 projected | original | Yoffe16(48) | S3 PSRT | 0.68 (0.02) | 45% (4%) | FigS20 |
| S3 projected | original | Yoffe16(55) | S3 PSRT | 0.67 (0.02) | 42% (3) | FigS20 |
| S3 projected | 16 km | Yoffe16(40) | S3 PSRT | 0.62 (0.01) | 32% (11%) | FigS21 |
| S6 projected | 16 km | Yoffe16(40) | S3 PSRT | 0.53 (0.02) | 15% (19%) | FigS21 |
| J3 projected | 16 km | Yoffe16(40) | S3 PSRT | 0.56 (0.03) | 23% (16%) | FigS21 |
| S3 projected | 16 km | Yoffe16(40) | S6 PSRT | 0.58 (0.02) | 32% (13%) | FigS22 |
| S3 projected | 16 km | Yoffe16(40) | J3 PSRT | 0.55 (0.02) | 28% (13%) | FigS22 |

[a] subfault size of the finite fault model, original S3 model subfault size is 25 km × 16.6 km

[b] Yoffe16(): Yoffe function with rise time 16s with duration in parentheses; Cosine16: Cosine function with rise time 16; Tri16: Triangle function with rise time 16. The slip-rate functions are shown in Figure S6

[c] Vr km/s - Rupture onset by constant rupture speed; Rupture onset - follow model rupture onset time; PSRT - peak slip rate time (Figure S5 and Figure S13).

[d] median (standard deviation)

[e] supplementary figure showing the synthetics and observed waveforms comparison

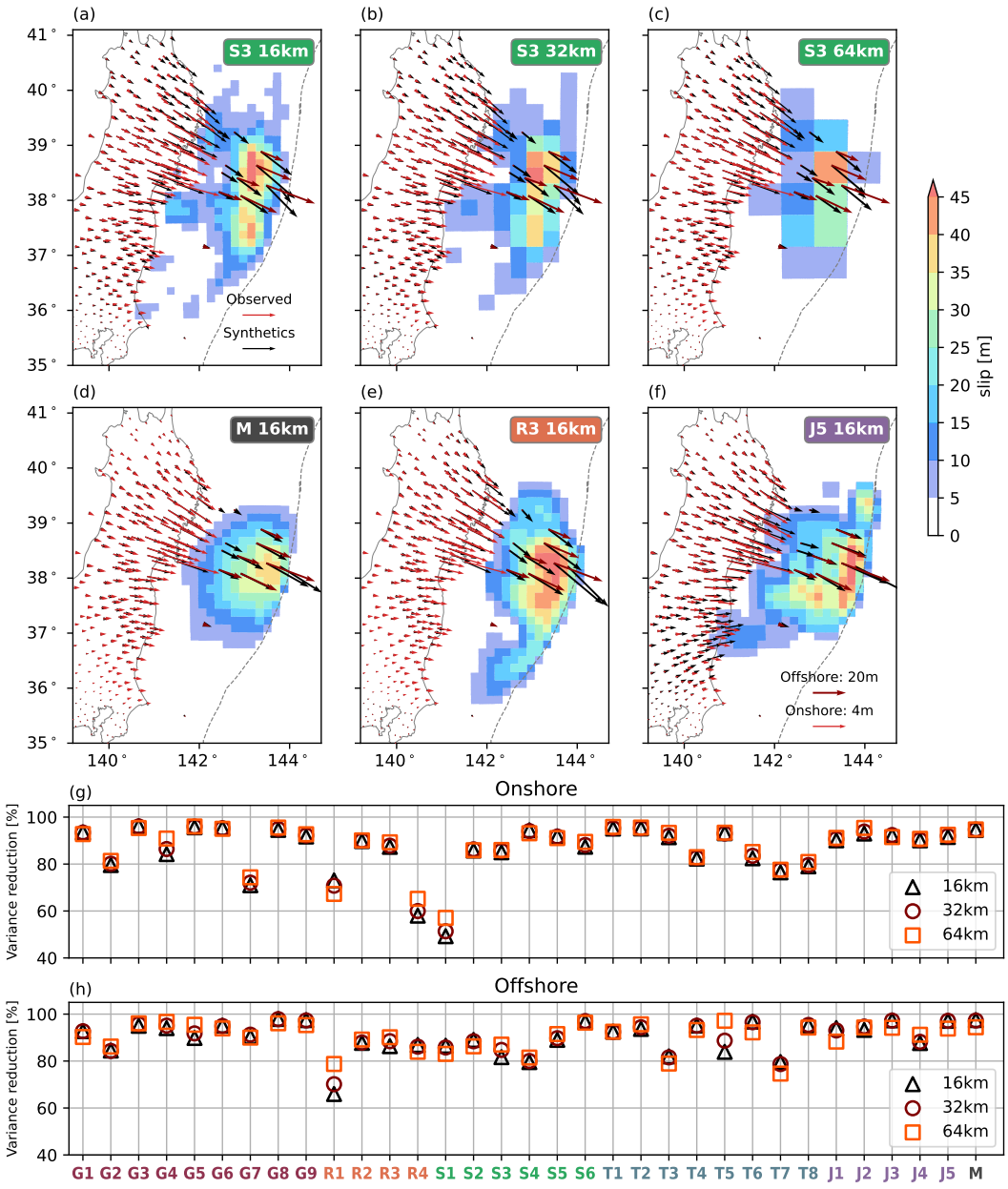


**Figure S1.** Onshore and offshore horizontal geodetic displacement observations (red arrows) and synthetics (black arrows), and their variance reduction values. (a)–(c) synthetic (black) and observed (red) horizontal geodetic displacements of model S3 at the 16 (a), 32 (b), and 64 km (c) scales. (d)–(f) geodetic synthetics and observations of model M (d), R3 (e), J5 (f) at the 16 km scale. (g) variance reduction values between the onshore geodetic synthetics and observations at the 16, 32, and 64 km scales. (h) variance reduction values between the offshore geodetic synthetics and observations at the 16, 32, and 64 km scales..

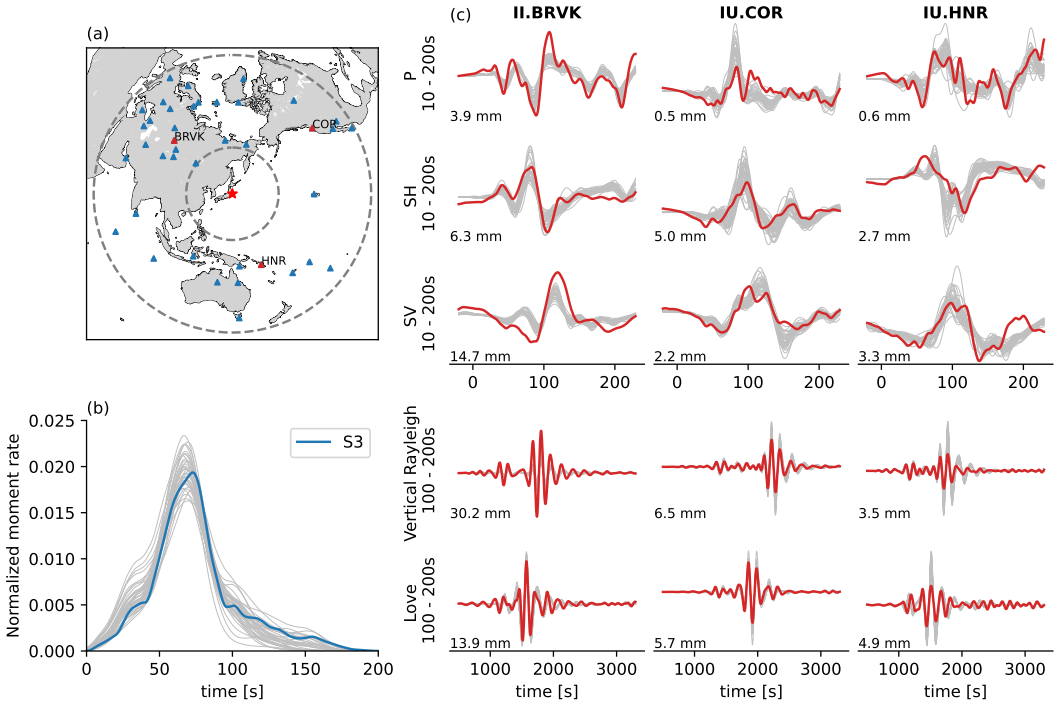


**Figure S2.** Comparison of teleseismic observations and synthetics at 32 km scale. (a) Map view of 40 II and IU stations used in the analysis. Red triangles are the stations in (c). Dotted circles show epicentral distances of $30^c irc$ and $90^c irc$, respectively. (b) Normalized moment rate functions of the original S3 model and the other 32 finite-fault models and the median model. (c) Synthetic and observed teleseismic waveforms. Red lines are the observed waveforms; grey lines are the synthetic waveforms from the 32 finite-fault models and the median model. Five rows are P wave, SH wave, SV wave, Rayleigh wave, and Love wave, respectively. Amplitudes of the observed waveforms are labeled at the lower-left corner of each waveform plot.

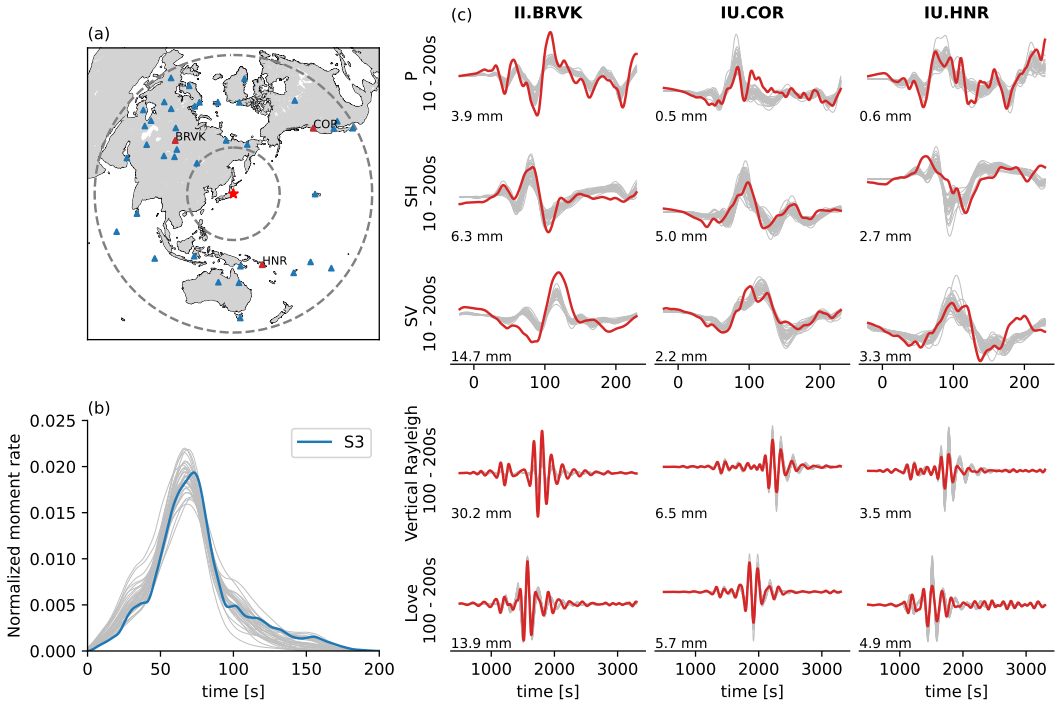


**Figure S3.** Comparison of teleseismic observations and synthetics a 64 km scale. (a) Map view of 40 II and IU stations used in the analysis. Red triangles are the stations in (c). Dotted circles show epicentral distances of $30^c irc$ and $90^c irc$, respectively. (b) Normalized moment rate functions of the original S3 model and the other 32 finite-fault models and the median model. (c) Synthetic and observed teleseismic waveforms. Red lines are the observed waveforms; grey lines are the synthetic waveforms from the 32 finite-fault models and the median model. Five rows are P wave, SH wave, SV wave, Rayleigh wave, and Love wave, respectively. Amplitudes of the observed waveforms are labeled at the lower-left corner of each waveform plot.

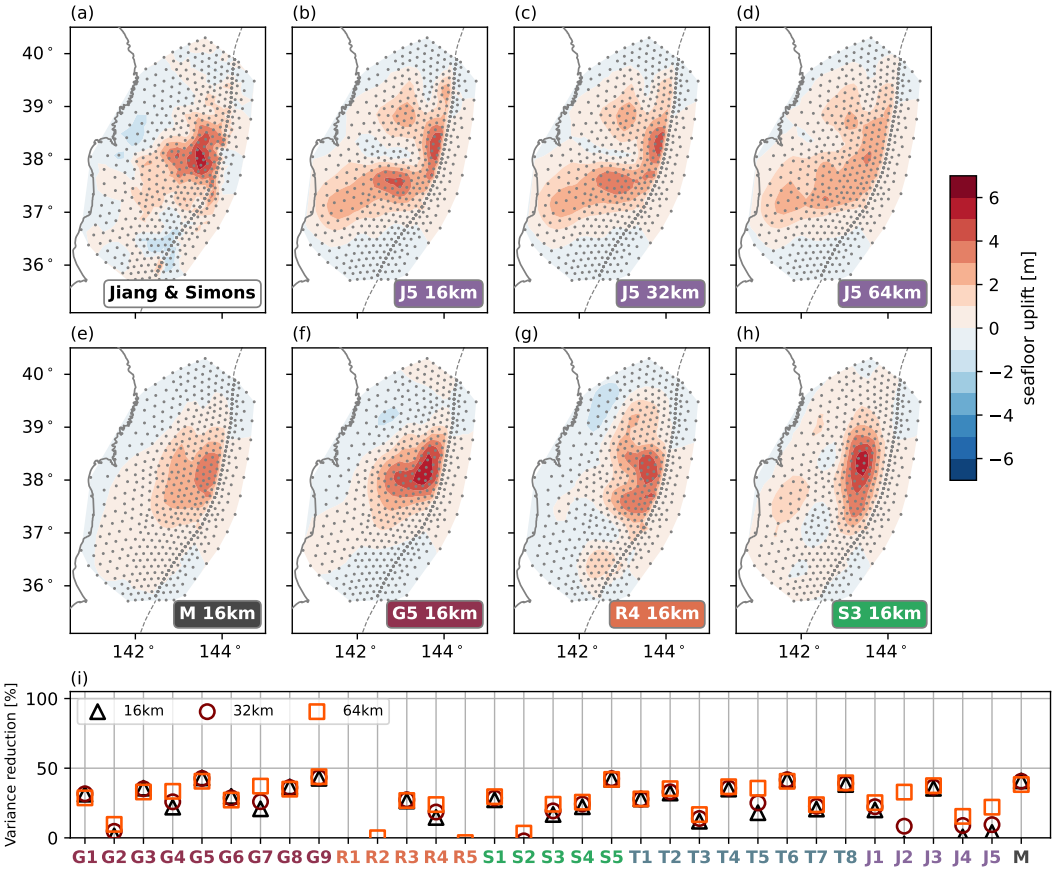


**Figure S4.** Seafloor uplift model of Jiang and Simons (2016) (model SJS), seafloor uplift synthetics from the finite-fault models, and their variance reduction values between the synthetics with model SJS. Grey dots show the modeled grid points. (a) Model SJS. (b)–(d) Synthetic seafloor uplift of model J5 model at the 16 (b), 32 (c), and 64 km (d) scales, respectively. (e)–(h) Synthetic seafloor uplift of the median slip model, models G5, R4, and S3 at a 16 km scale. (i) variance reduction values between model SJS and synthetics of the 32 finite-fault models and the median model at the 16, 32, and 64 km scales.

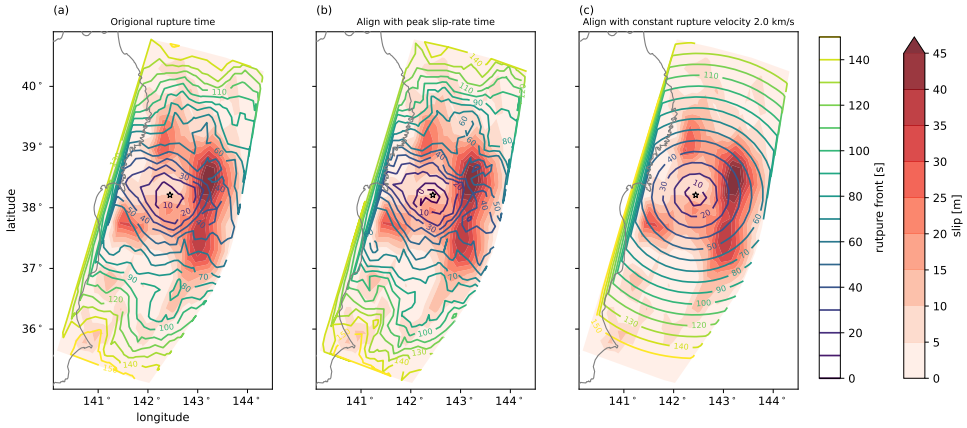


**Figure S5.** Rutpure onset time alignment for the teleseismic synthetics. Panel a shows the original rupture onset time of the S3 model. Panel b shows the alignment with the peak-slip-rate time (PSRT) of the S3 model. Panel c shows the alignment with the constant 2.0 m/s rupture velocity.

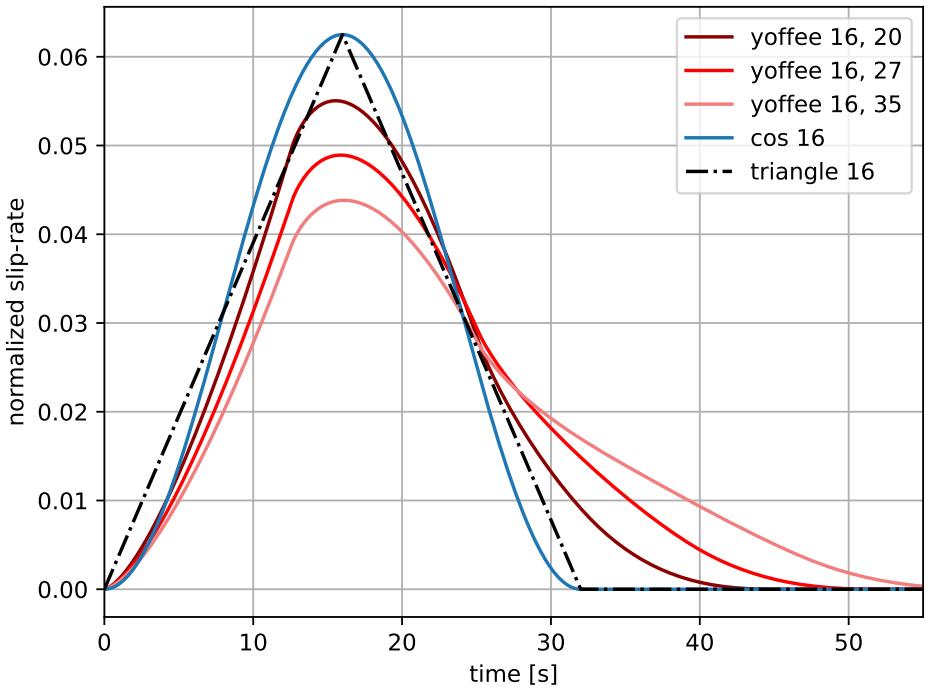


**Figure S6.** Normalized slip-rate functions evaluated in the teleseismic synthetics. Slip-rate functions include three sets of Yoffe slip-rate functions (reds) with the same rise-time of 16 s and varying duration of 40, 48, and 55 s, and a cosine function with a 16 s rise time (blue) and a symmetrical-triangular function with a rise time of 16 s (grey).

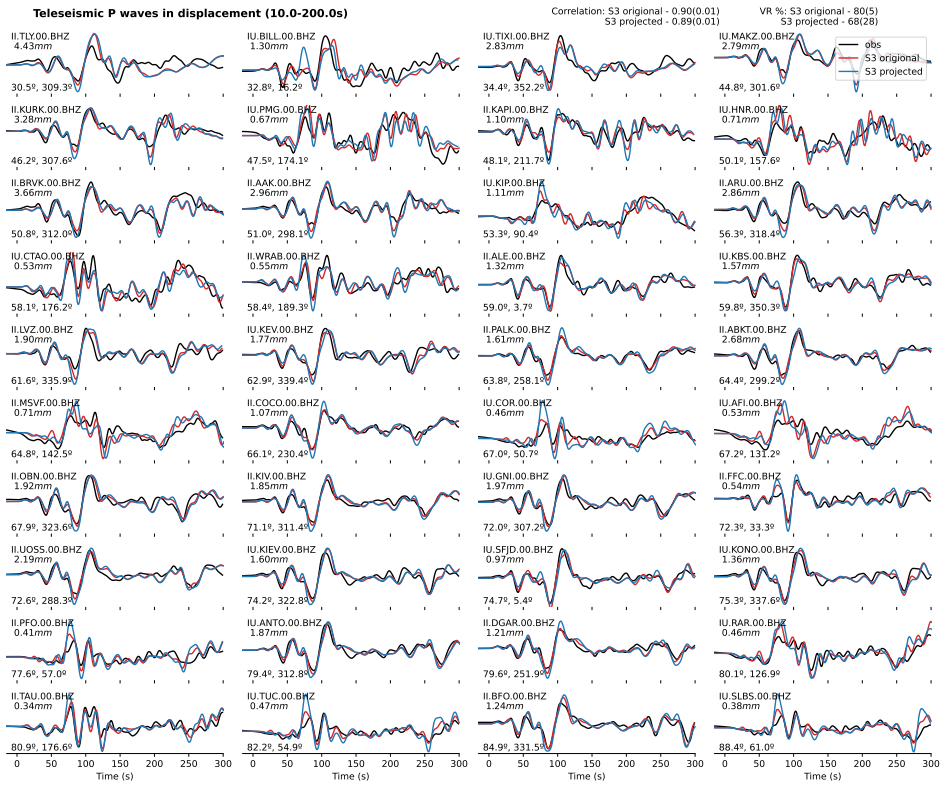


**Figure S7.** Comparison of the Teleseismic P wave on changing fault geometry. P wave synthetics of the S3 original model (red) and S3 projected model (blue) and observations (black) for all 40 stations in Figure 11. The waveform is filtered between 10–200s period and aligned with maximum cross-correlation value. Overall correlation and variance reduction value with the observations are labeled at the top-right corner of the figure. Medians and standard deviations of the correlation value of the original model and projected model synthetics are 0.9 and 0.01, and 0.89 and 0.01, respectively. The median variance reduction of the original model is 80%, and the projected model is 68%, respectively. Distance in degree and back azimuth of the station are shown at the bottom-left corner of each waveform plot. Station trace ID and amplitude are labeled at the upper-left corner of each waveform plot.

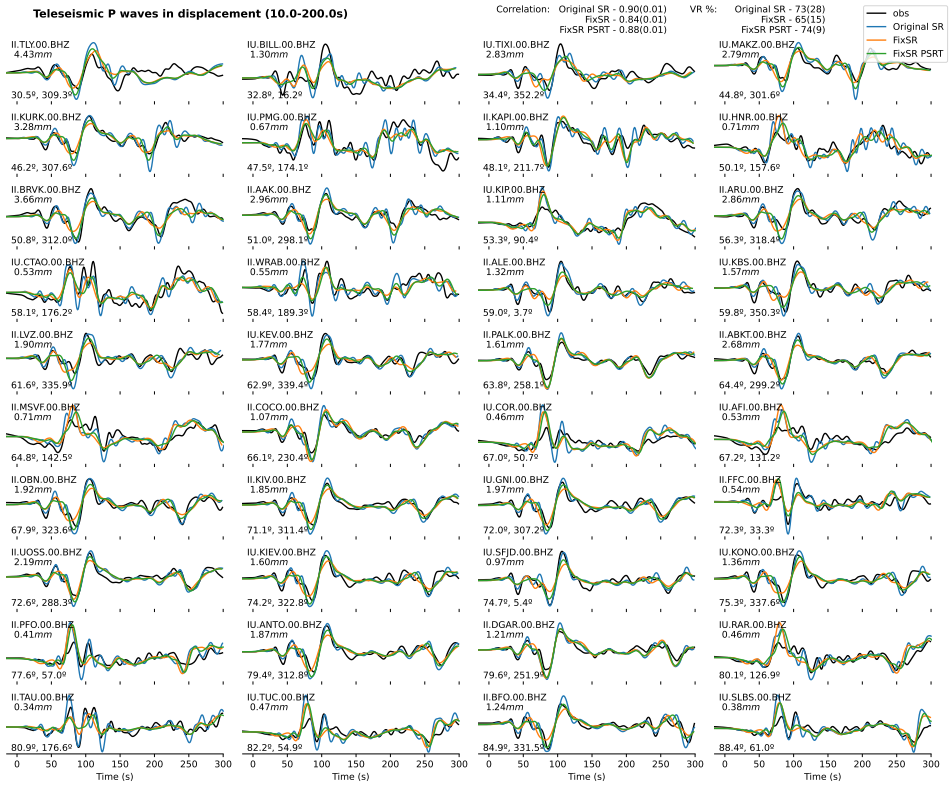


**Figure S8.** Comparison of the Teleseismic P wave on unifying slip rate function with Yoffe function and rupture front alignment. Same plotting as Figure S7. P wave synthetics of the S3 projected model [S3p] (blue), S3 projected unified slip rate model [S3p FixSR](orange), S3 projected unified slip rate model aligned with S3 peak slip rate time [S3p FixSR PSRT](green) and observations (black) of all 40 stations.

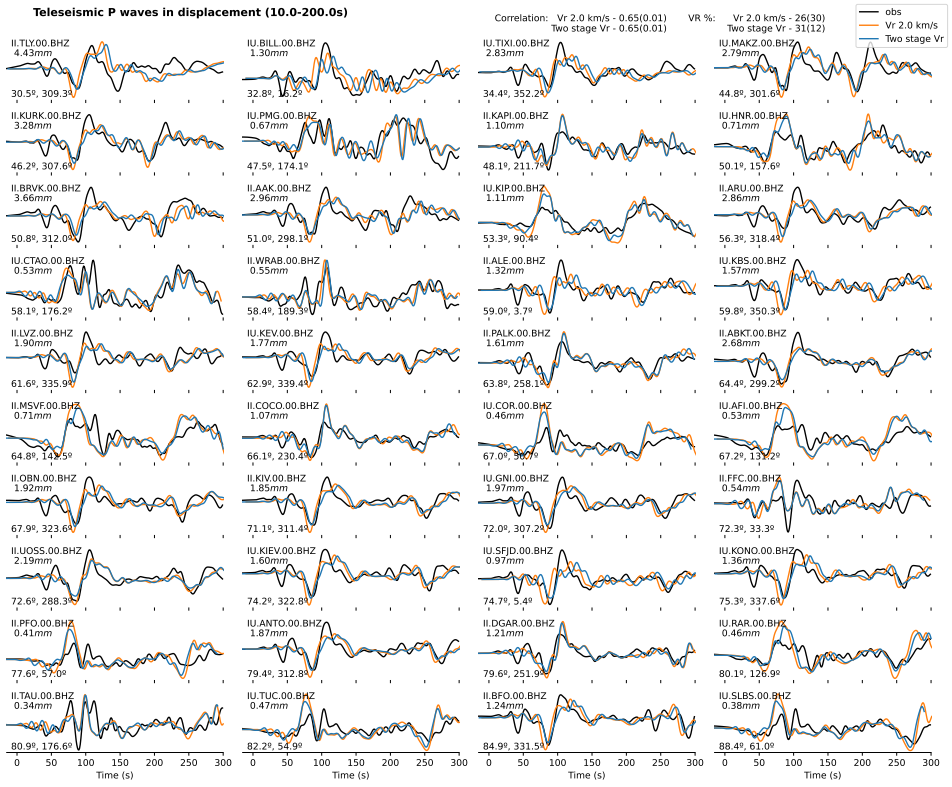


**Figure S9.** Comparison of the Teleseismic P wave on aligning rupture onset with constant rupture velocity. Same plotting as Figure S7. S3 projected with fix 2.0 km/s rupture velocity model [S3p Vr 20km/s](blue), P wave synthetics with two steps 1.5 km/s and 2.0 km/s rupture velocity model [orange] (blue) and and observations (black) of all 40 stations.

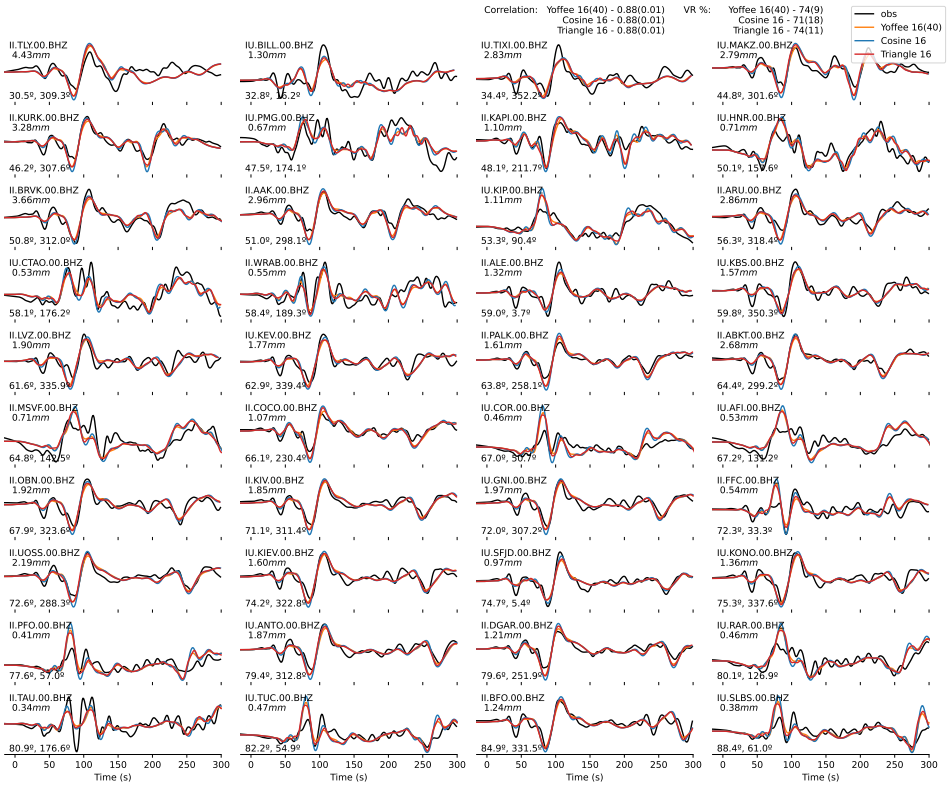


**Figure S10.** Comparison of the Teleseismic P wave with varying slip-rate function. Same plotting as Figure S7. P wave synthetics with Yoffe slip-rate function (orange), synthetics with cosine slip-rate function (blue), synthetics with triangular slip-rate function (red), and observations (black) of all 40 stations.

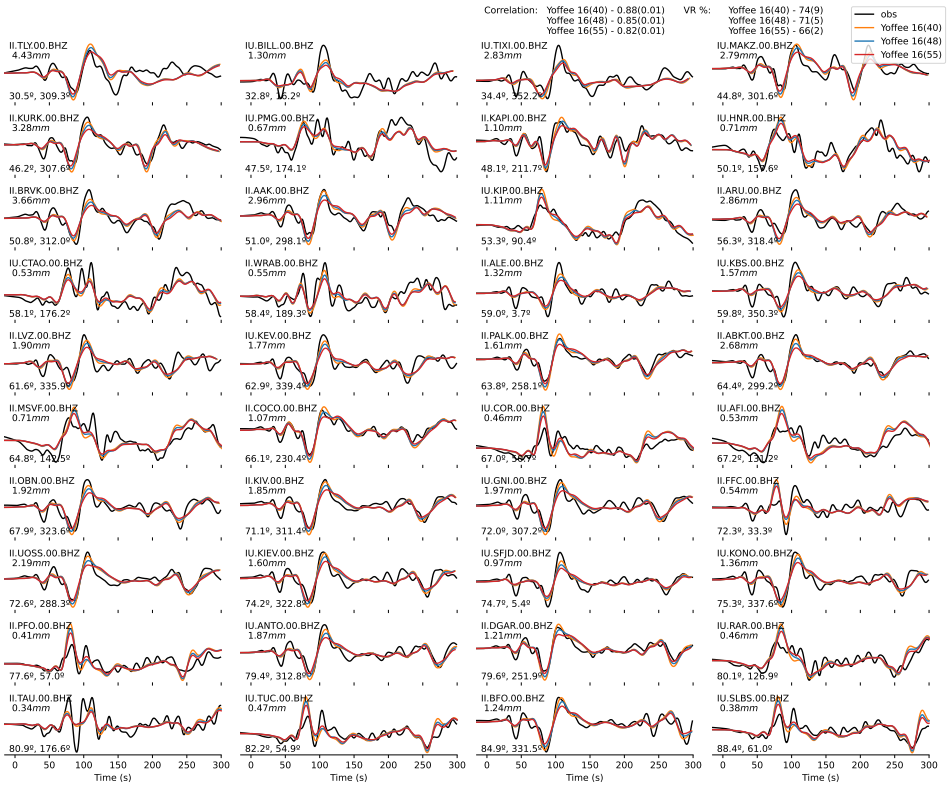


**Figure S11.** Comparison of the Teleseismic P wave with varying Yoffe slip-rate function. Same plotting as Figure S7. P wave synthetics with Yoffe function rise time and duration of 16 and 40 s (orange), synthetic with Yoffe function rise time and duration of 16 and 48s (blue), synthetics with Yoffe function rise time and duration of 16 and 55s (red), and observations (black) of all 40 stations.

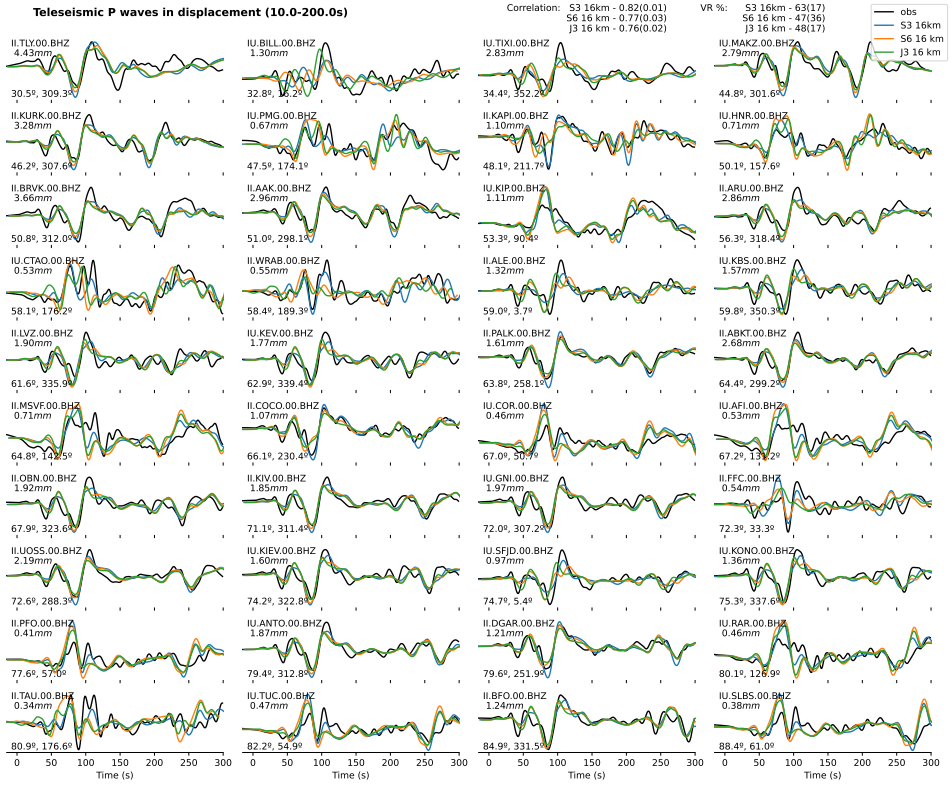


**Figure S12.** Comparison of the Teleseismic P wave with slip model S3, S6 and J3 at 16 km resolution. Same plotting as Figure S7. P wave synthetics of slip model S3 (blue), synthetics of slip model S6 (orange), synthetics of slip model J3 (green), and observations (black) of all 40 stations.

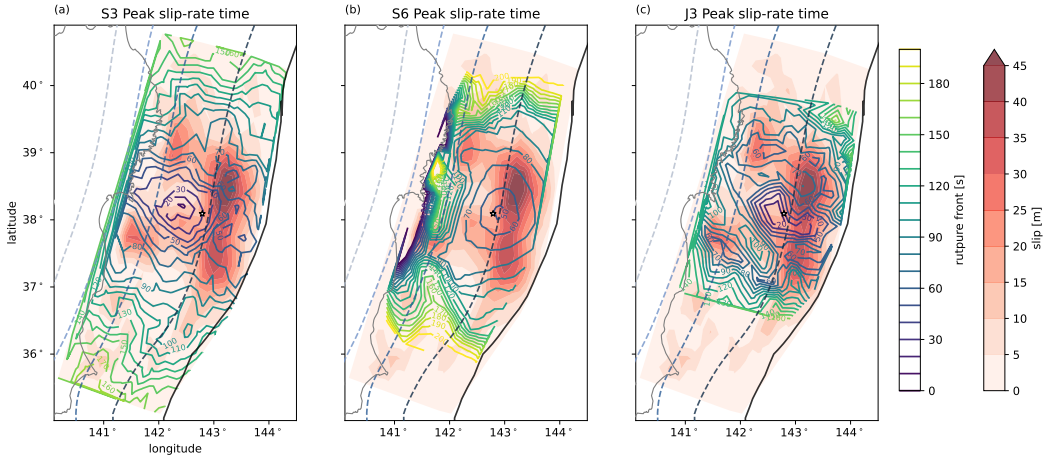


**Figure S13.** Comparing models peak slip-rate time. Color contours show the (a) S3, (b) S6, and (c) J3 models' peak slip-rate time, respectively. Model S3 slip distribution is shown as the color-filled contour. The peak slip-rate time of models S6 and J3 are spatially limited due to the different fault parameterization of these two models. Hypocenters of these models are also shifted due to the projection onto the realistic geometry

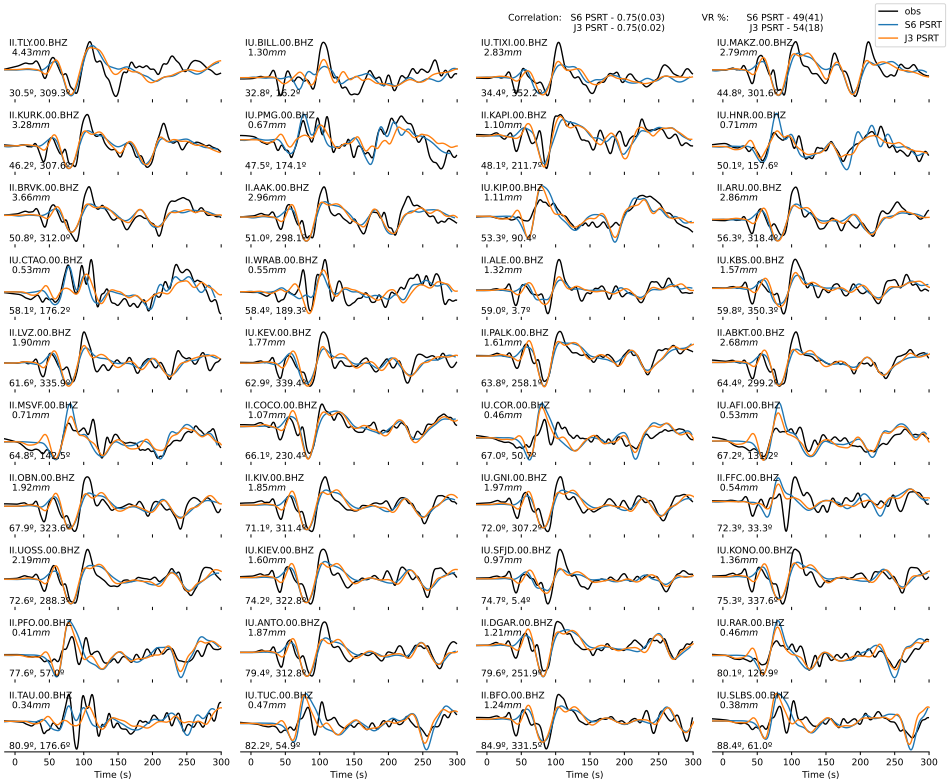


**Figure S14.** Comparison of the Teleseismic P wave with rupture front alignment with the peak-slip-rate time of S6 and J3 models with S3 slip model at 16 km resolution. Same plotting as Figure S7. P wave synthetics with rupture front align with S6 peak-slip-rate time (blue), synthetics with rupture front align with J3 peak-slip-rate time (orange), and observations (black) of all 40 stations.

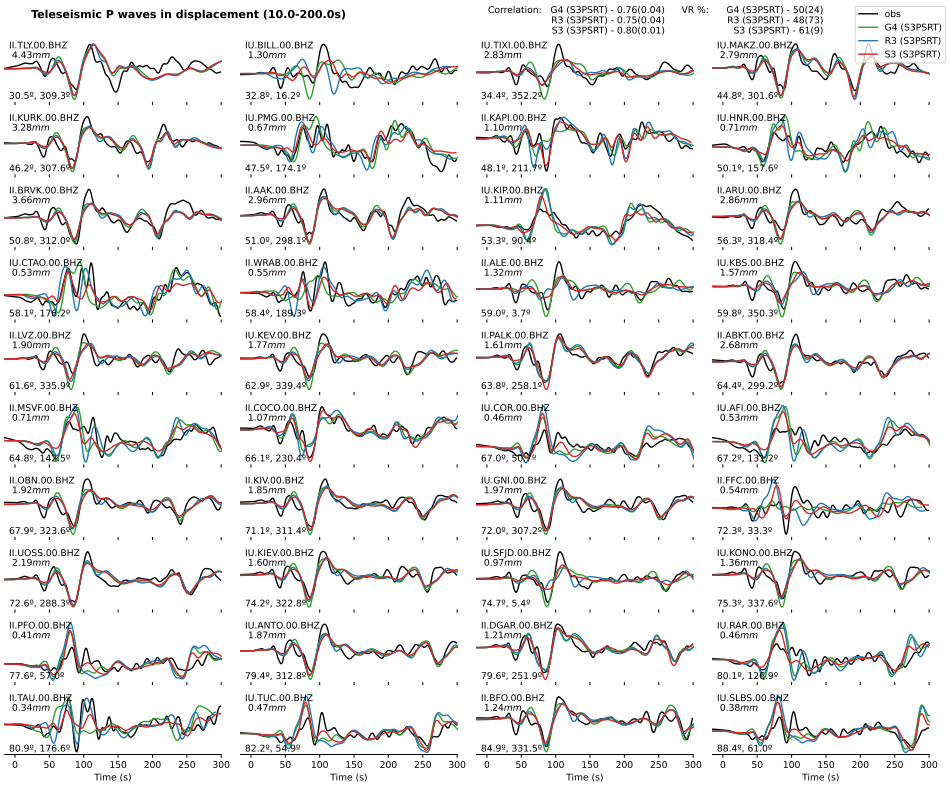


**Figure S15.** Comparison of the Teleseismic P wave with slip model G4, R3 and S3 at 16 km resolution. Same plotting as Figure S7. P wave synthetics with G4 model slip distribution (green), synthetics with R3 model slip distribution (blue), synthetics with S3 model slip distribution (red), and observations (black) of all 40 stations.

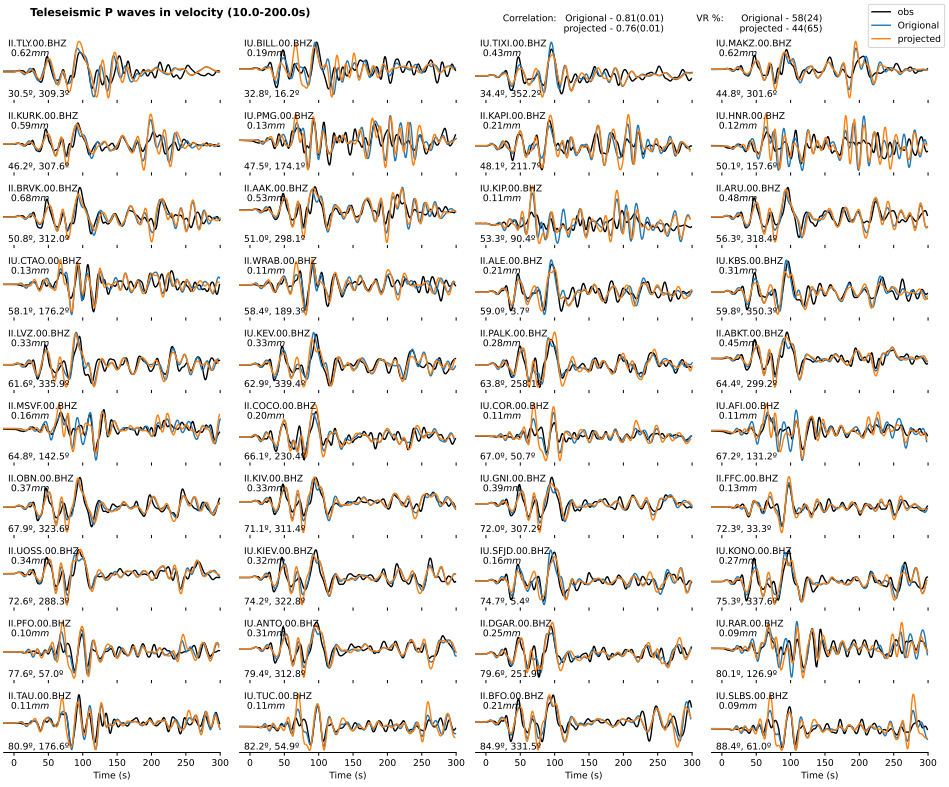


**Figure S16.** Comparison of the Teleseismic velocity P wave with original S3 finite-fault model and projected S3 finite-fault model. Same plotting as Figure S7. P wave synthetics of the original S3 finite-fault model (blue), synthetics of the projected S3 finite-fault model (orange), and observations (black) of all 40 stations.

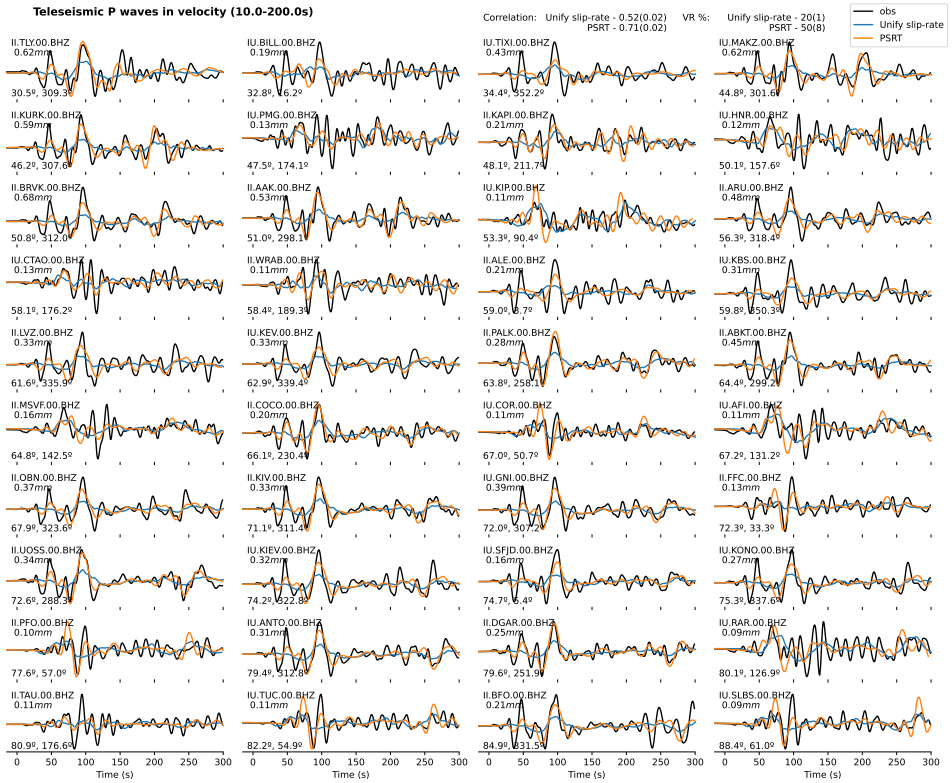


**Figure S17.** Comparison of the Teleseismic velocity P wave with unified slip-rate function with original onset-time alignment and peak-slip-rate time alignment. Same plotting as Figure S7. P wave synthetics of unified slip-rate function with original onset-time alignment (blue), synthetics of unified slip-rate function with peak-slip-rate time alignment (orange), observations (black) of all 40 stations.

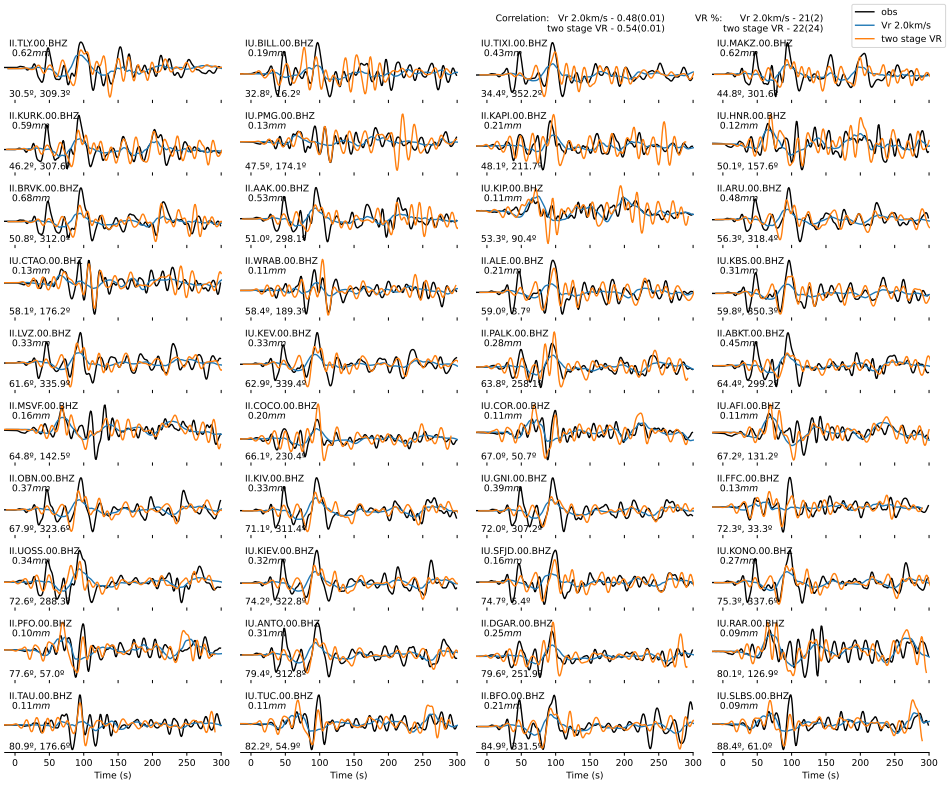


**Figure S18.** Comparison of the Teleseismic velocity P wave with onset-time alignment with constant rupture speed of 2.0 km/s and two-step rupture speed with S3 slip distribution. Same plotting as Figure S7. P wave synthetics of constant rupture speed of 2.0 km/s (blue), synthetics of two-step rupture speed (orange), observations (black) of all 40 stations.

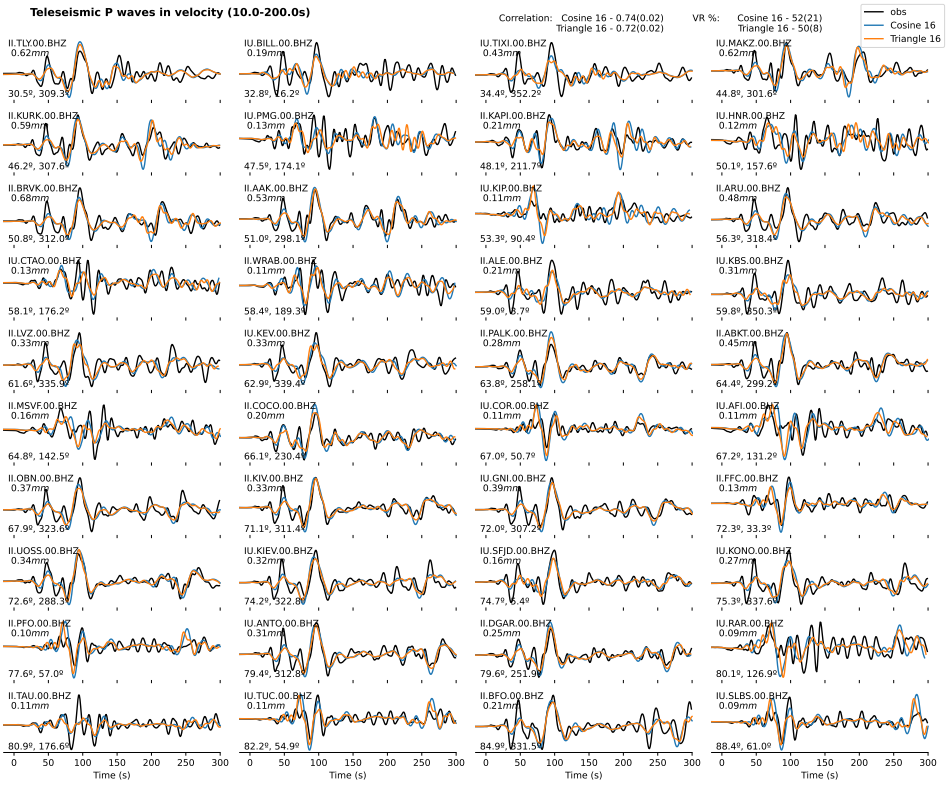


**Figure S19.** Comparison of the Teleseismic velocity P wave with cosine slip-rate function and triangular slip-rate function. Same plotting as Figure S7. P wave synthetics of cosine slip-rate function (blue), synthetics of triangle slip-rate function (orange), observations (black) of all 40 stations.

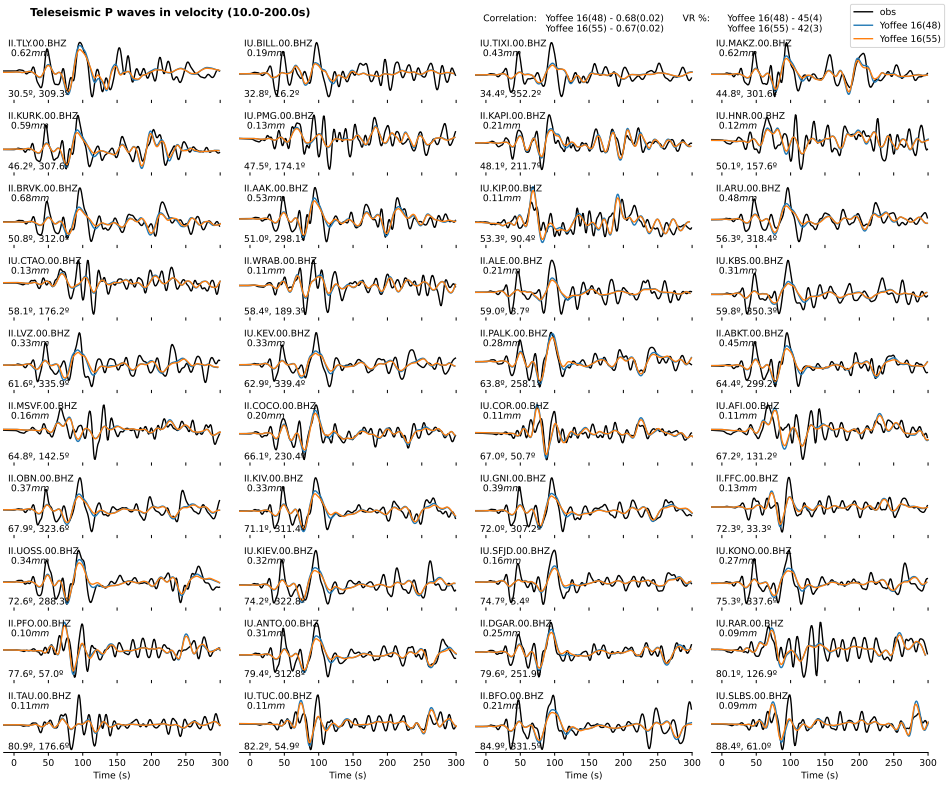


**Figure S20.** Comparison of the Teleseismic velocity P wave with varying Yoffe function. Same plotting as Figure S7. P wave synthetics of the Yoffe function with 48s duration (blue), synthetics of the Yoffe function with 55s duration (orange), and observations (black) of all 40 stations.

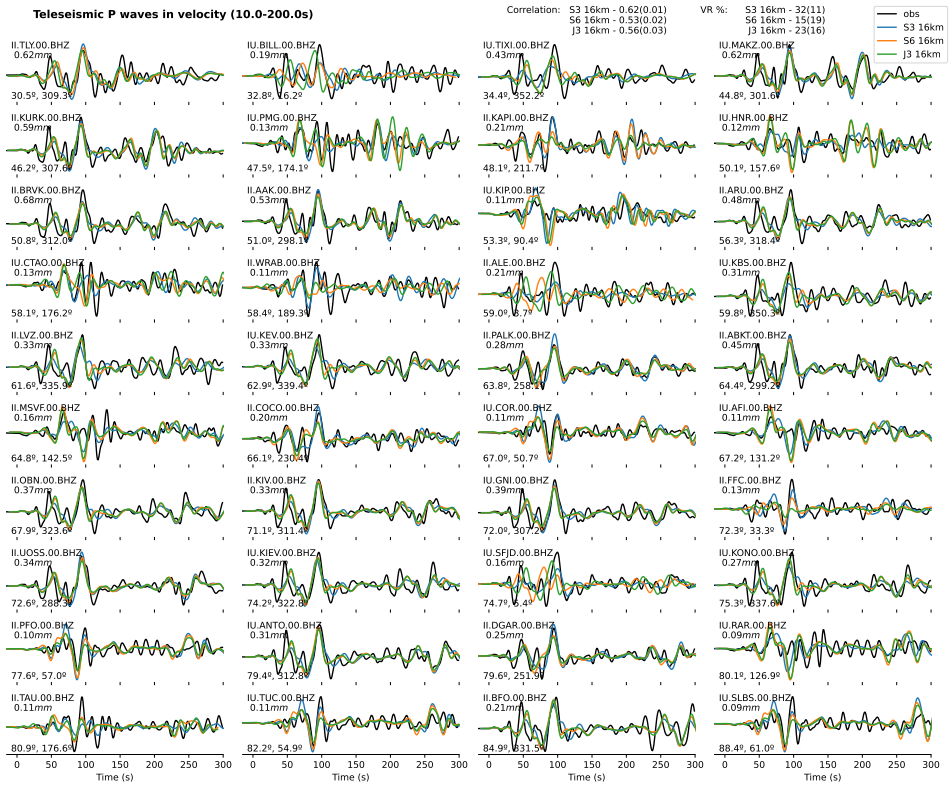


**Figure S21.** Comparison of the Teleseismic velocity P wave with different model slip distribution and S3 model PSRT onset-time alignment. Same plotting as Figure S7. P wave synthetics of S3 slip model (blue), synthetics of S6 slip model (orange), synthetics of J3 slip model (green), and observations (black) of all 40 stations.

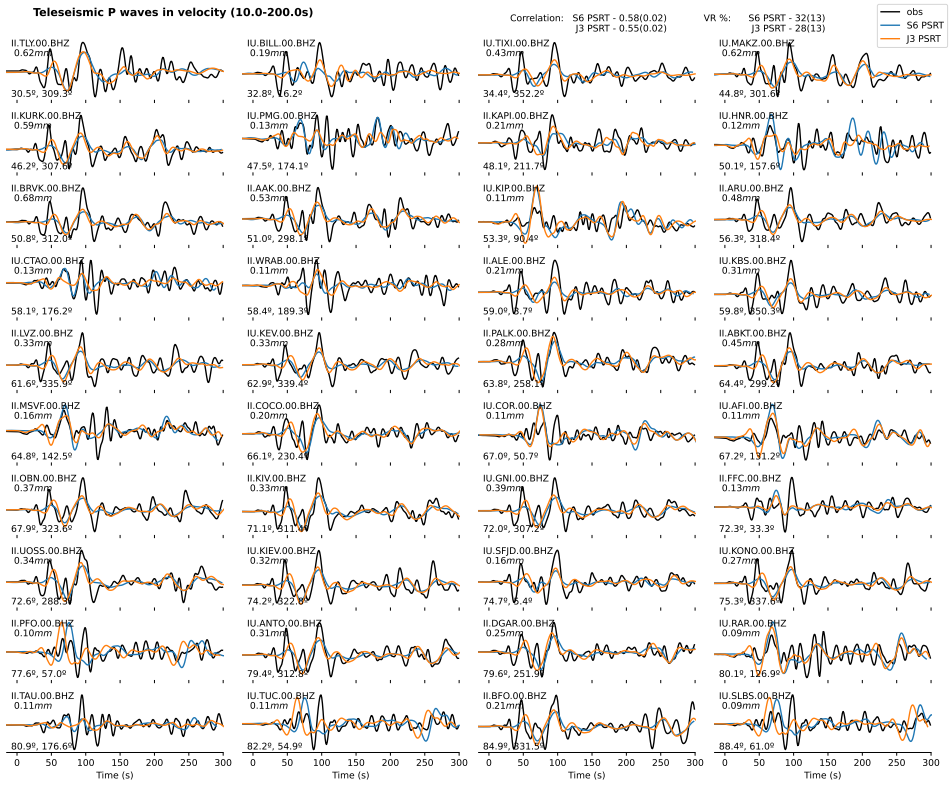


**Figure S22.** Comparison of the Teleseismic velocity P wave with different model PSRT onset-time alignment and S3 model slip distribution. Same plotting as Figure S7. P wave synthetics of S6 model PSRT (blue), synthetics of J3 model PSRT (orange), and observations (black) of all 40 stations.

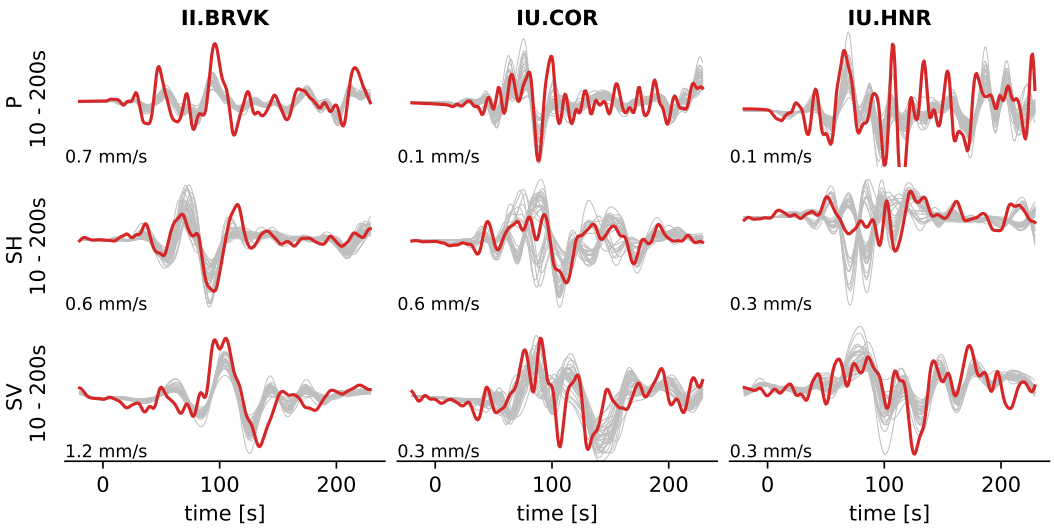


**Figure S23.** Comparison of teleseismic velocity observations and synthetics a 16 km scale. Synthetic and observed teleseismic waveforms. Red lines are the observed waveforms; grey lines are the synthetic waveforms from the 32 finite-fault models and the median model. Three rows are P wave, SH wave and SV wave, respectively. Amplitudes of the observed waveforms are labeled at the lower-left corner of each waveform plot.

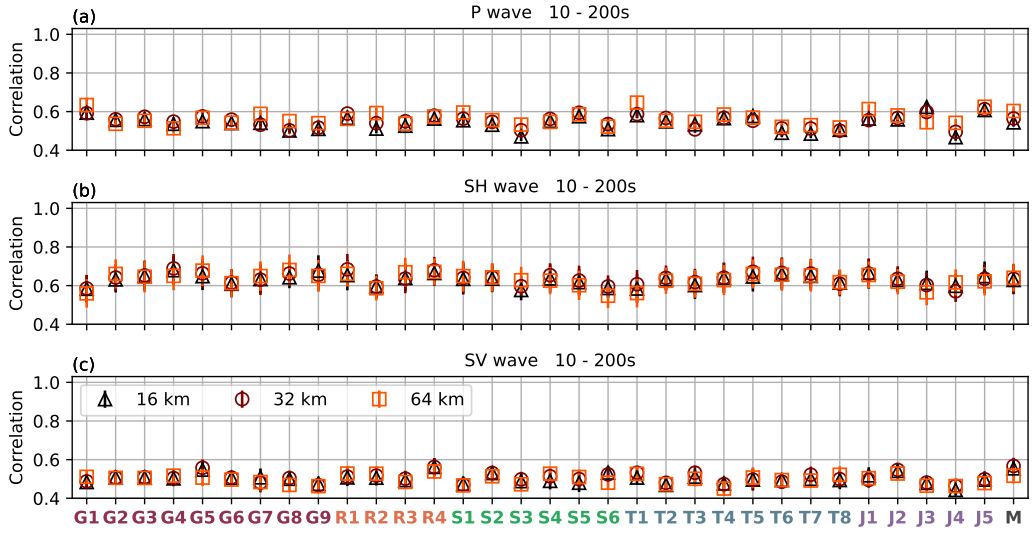


**Figure S24.** Correlation coefficient values between the teleseismic velocity observations and synthetics at the 16, 32, and 64 km scales. (a) P wave. (b) SH wave. (c) SV wave. Median correlation values between the synthetic and observed teleseismic waveforms at the 40 teleseismic stations are taken as the characteristic correlation coefficient values for each model. Three markers indicate the characteristic median values for models at the 16, 32, and 64 km scales. Error bars represent the associated standard deviation of correlation coefficient values of the 40 stations.

## References


Ammon, C. J., Lay, T., Kanamori, H., & Cleveland, M. (2011). A rupture model of the 2011 off the Pacific coast of Tohoku earthquake. *Earth, Planets and Space*, *63*(7), 693–696.

Bletery, Q., Sladen, A., Delouis, B., Vallée, M., Nocquet, J.-M., Rolland, L., & Jiang, J. (2014). A detailed source model for the $M_w$ 9.0 Tohoku-Oki earthquake reconciling geodesy, seismology, and tsunami records. *Journal of Geophysical Research: Solid Earth*, *119*(10), 7636–7653.

Diao, F., Xiong, X., & Zheng, Y. (2012). Static slip model of the m w 9.0 Tohoku (Japan) earthquake: Results from joint inversion of terrestrial GPS data and seafloor GPS/acoustic data. *Chinese Science Bulletin*, *57*, 1990–1997.

Fujii, Y., Satake, K., Sakai, S., Shinohara, M., & Kanazawa, T. (2011). Tsunami source of the 2011 off the Pacific coast of Tohoku earthquake. *Earth, planets and space*, *63*(7), 815–820.

Goldberg, D., Barnhart, W., & Crowell, B. (2022). Regional and teleseismic observations for finite-fault product. *US Geol. Surv. Data Release*.

Gusman, A. R., Tanioka, Y., Sakai, S., & Tsushima, H. (2012). Source model of the great 2011 Tohoku earthquake estimated from tsunami waveforms and crustal deformation data. *Earth and Planetary Science Letters*, *341*, 234–242.

Hashima, A., Becker, T. W., Freed, A. M., Sato, H., & Okaya, D. A. (2016). Coseismic deformation due to the 2011 Tohoku-Oki earthquake: influence of 3-D elastic structure around Japan. *Earth, Planets and Space*, *68*(1), 1–15.

Hayes, G. P. (2011, 09). Rapid source characterization of the 2011 $M_w$ 9.0 off the Pacific coast of Tohoku earthquake. *Earth, Planets and Space*, *63*(7), 529-534.

Hooper, A., Pietrzak, J., Simons, W., Cui, H., Riva, R., Naeije, M., ... Socquet, A. (2013). Importance of horizontal seafloor motion on tsunami height for the 2011 $M_w$= 9.0 Tohoku-Oki earthquake. *Earth and Planetary Science Letters*, *361*, 469–479.

Ide, S., Baltay, A., & Beroza, G. C. (2011). Shallow dynamic overshoot and energetic deep rupture in the 2011 $M_w$ 9.0 Tohoku-Oki earthquake. *Science*, *332*(6036), 1426–1429.

Iinuma, T., Hino, R., Kido, M., Inazu, D., Osada, Y., Ito, Y., ... others (2012). Coseismic slip distribution of the 2011 off the Pacific Coast of Tohoku earthquake (M9.0) refined by means of seafloor geodetic data. *Journal of Geophysical Research: Solid Earth*, *117*(B7).

Ito, T., Ozawa, K., Watanabe, T., & Sagiya, T. (2011). Slip distribution of the 2011 off the Pacific coast of Tohoku earthquake inferred from geodetic data. *Earth, planets and space*, *63*(7), 627–630.

Jiang, J., & Simons, M. (2016). Probabilistic imaging of tsunamigenic seafloor deformation during the 2011 Tohoku-Oki earthquake. *Journal of Geophysical Research: Solid Earth*, *121*(12), 9050–9076.

Kubo, H., & Kakehi, Y. (2013). Source process of the 2011 Tohoku earthquake estimated from the joint inversion of teleseismic body waves and geodetic data including seafloor observation data: source model with enhanced reliability by using objectively determined inversion settings. *Bulletin of the Seismological Society of America*, *103*(2B), 1195–1220.

Kubota, T., Saito, T., & Hino, R. (2022). A new mechanical perspective on a shallow megathrust near-trench slip from the high-resolution fault model of the 2011 Tohoku-Oki earthquake. *Progress in Earth and Planetary Science*, *9*(1), 1–19.

Lee, S.-J., Huang, B.-S., Ando, M., Chiu, H.-C., & Wang, J.-H. (2011). Evidence of large scale repeating slip during the 2011 Tohoku-Oki earthquake. *Geophysical Research Letters*, *38*(19).

Melgar, D., & Bock, Y. (2015). Kinematic earthquake source inversion and tsunami runup prediction with regional geophysical data. *Journal of Geophysical Re-*

*search: Solid Earth*, *120*(5), 3324–3349.

Minson, S. E., Simons, M., Beck, J., Ortega, F., Jiang, J., Owen, S., ... Sladen, A. (2014). Bayesian inversion for finite fault earthquake source models–*ii*: the 2011 great Tohoku-Oki, Japan earthquake. *Geophysical Journal International*, *198*(2), 922–940.

Pollitz, F. F., Bürgmann, R., & Banerjee, P. (2011). Geodetic slip model of the 2011 M9.0 Tohoku earthquake. *Geophysical Research Letters*, *38*(7).

Romano, F., Trasatti, E., Lorito, S., Piromallo, C., Piatanesi, A., Ito, Y., ... Cocco, M. (2014). Structural control on the Tohoku earthquake rupture process investigated by 3d FEM, tsunami and geodetic data. *Scientific reports*, *4*(1), 1–11.

Saito, T., Ito, Y., Inazu, D., & Hino, R. (2011). Tsunami source of the 2011 Tohoku-Oki earthquake, Japan: Inversion analysis based on dispersive tsunami simulations. *Geophysical Research Letters*, *38*(7).

Satake, K., Fujii, Y., Harada, T., & Namegaya, Y. (2013). Time and space distribution of coseismic slip of the 2011 Tohoku earthquake as inferred from tsunami waveform data. *Bulletin of the seismological society of America*, *103*(2B), 1473–1492.

Simons, M., Minson, S. E., Sladen, A., Ortega, F., Jiang, J., Owen, S. E., ... others (2011). The 2011 magnitude 9.0 Tohoku-Oki earthquake: Mosaicking the megathrust from seconds to centuries. *science*, *332*(6036), 1421–1425.

Suzuki, W., Aoi, S., Sekiguchi, H., & Kunugi, T. (2011). Rupture process of the 2011 Tohoku-Oki mega-thrust earthquake (M9. 0) inverted from strong-motion data. *Geophysical Research Letters*, *38*(7).

Wang, C., Ding, X., Shan, X., Zhang, L., & Jiang, M. (2012). Slip distribution of the 2011 Tohoku earthquake derived from joint inversion of GPS, InSAR and seafloor GPS/acoustic measurements. *Journal of Asian Earth Sciences*, *57*, 128–136.

Wang, R., Parolai, S., Ge, M., Jin, M., Walter, T. R., & Zschau, J. (2013). The 2011 $M_w$ 9.0 Tohoku earthquake: Comparison of GPS and strong-motion data. *Bulletin of the Seismological Society of America*, *103*(2B), 1336–1347.

Wei, S., Graves, R., Helmberger, D., Avouac, J.-P., & Jiang, J. (2012). Sources of shaking and flooding during the Tohoku-Oki earthquake: A mixture of rupture styles. *Earth and Planetary Science Letters*, *333*, 91–100.

Xie, Z., & Cai, Y. (2018). Inverse method for static stress drop and application to the 2011 $M_w$9. 0 Tohoku-Oki earthquake. *Journal of Geophysical Research: Solid Earth*, *123*(4), 2871–2884.

Yagi, Y., & Fukahata, Y. (2011). Rupture process of the 2011 Tohoku-Oki earthquake and absolute elastic strain release. *Geophysical Research Letters*, *38*(19).

Yamazaki, Y., Cheung, K. F., & Lay, T. (2018). A self-consistent fault slip model for the 2011 Tohoku earthquake and tsunami. *Journal of Geophysical Research: Solid Earth*, *123*(2), 1435–1458.

Yokota, Y., Koketsu, K., Fujii, Y., Satake, K., Sakai, S., Shinohara, M., & Kanazawa, T. (2011). Joint inversion of strong motion, teleseismic, geodetic, and tsunami datasets for the rupture process of the 2011 Tohoku earthquake. *Geophysical Research Letters*, *38*(7).

Yue, H., & Lay, T. (2013). Source rupture models for the $M_w$ 9.0 2011 Tohoku earthquake from joint inversions of high-rate geodetic and seismic data. *Bulletin of the Seismological Society of America*, *103*(2B), 1242–1255.

Zhou, X., Cambiotti, G., Sun, W., & Sabadini, R. (2014). The coseismic slip distribution of a shallow subduction fault constrained by prior information: the example of 2011 Tohoku ($M_w$ 9.0) megathrust earthquake. *Geophysical Journal International*, *199*(2), 981–995.